Published in final edited form as:
J Org Chem. 2013 October 18; 78(20): 10288–10297. doi:10.1021/jo401665n.

A Computational Study of the Copper(II) Catalyzed Enantioselective Intramolecular Aminooxygenation of Alkenes

Lee Belding, **Sherry Chemler**[‡], and **Travis Dudding**[*]

[*]Brock University, St. Catharines, Ontario, L2S 3A1, Canada

[‡]Department of Chemistry, The State University of New York at Buffalo, Buffalo, New York 14260, United States

Abstract

The origin of enantioselectivity in the [Cu(*R*,*R*)-Ph-box](OTf)$_2$-catalyzed intramolecular aminooxygenation of *N*-sulfonyl-2-allylanilines and 4-pentenylsulfonamides to afford chiral indolines and pyrrolidines, respectively, was investigated using Density Functional Theory (DFT) calculations. The pyrrolidine-forming transition state model for the major enantiomer involves a chair-like seven-membered cyclization transition state with a distorted square planar copper center, while the transition state model for the minor enantiomer was found to have a boat-like cyclization geometry having a distorted tetrahedral geometry about the copper center. Similar copper-geometry trends were observed in the chiral indoline-forming reactions. These models were found to be qualitatively consistent with experimental results and allowed for rationalization of how substitution of the substrate backbone and *N* sulfonyl substituent affected the level of enantioselectivity in these and related copper(II)-catalyzed enantioselective reactions.

Keywords

Density Functional Theory; copper-catalyzed; alkene aminooxygenation; oxyamination; enantioselective; tetrahedral twist angle

INTRODUCTION

The development of catalytic enantioselective alkene difunctionalization reactions is an important and burgeoning area of chemical research.[1-5] Powerful transformations such as alkene dihydroxylation[3] and alkene aminohydroxylation,[5] for example, enable the concise, enantioselective synthesis of valuable chiral intermediates for use in fine chemical and natural product synthesis. Transition metal catalysis has played a prominent role in the development of enantioselective alkene difunctionalization reactions.[1-5] Over the past several years enantioselective alkene difunctionalization reactions catalyzed by copper(II) 2,2'-isopropylidenebis[(4*R*)-4-phenyl-2-oxazoline]ditriflate, [Cu(*R*,*R*)-Ph-box](OTf)$_2$, and copper(II) 2,2'-isopropylidenebis[(4*R*,5*S*)-4,5-diphenyl-2-oxazoline]ditriflate, [Cu(4*R*,5*S*)-di-Ph-box](OTf)$_2$, have been reported.[6-14] These chiral copper catalysts are well-known in the area of asymmetric catalysis[15,16] and their attributes include their generally robust nature and well-defined composition.[17] Despite their wide availability, their use as catalysts in the

tdudding@brocku.ca.

SUPPORTING INFORMATION

Relative energies for transition states **TS-1**, **TS-2**, **TS-3**, **TS-4**, and **TS-5** arising from single point calculations, AIM data and calculated structures for **TS-4S** and **TS-5S**, as well as input parameters, thermochemical data, and coordinates of all computed structures. This material is available free of charge via the Internet at http://pubs.acs.org.

enantioselective difunctionalization of alkenes is a relatively recent development. Many of the copper-catalyzed alkene difunctionalization reactions reported involve the cyclization of a sulfonamide nitrogen onto a pendant alkene (usually terminal) to form a new stereocenter in good to excellent enantiomeric excess.[6-13] These reactions include the aminooxygenation, carboamination, aminohalogenation, and hydroamination of alkenes.[6-13] Some of these reactions are summarized in eqs. 1-5. It is noteworthy that in these examples the reaction conditions (type of reaction), the backbone substituents of the substrate, and the *N*-sulfonyl substituent can all affect the level of enantioselectivity. Although a detailed transition state model, supported by DFT calculations, has been proposed to rationalize the diastereoselectivity obtained in the copper(II) carboxylate-promoted aminooxygenation reactions of α substituted-γ-pentenyl sulfonamides,[18-20] still lacking is a well-developed understanding of the origin of enantioselectivity in the [Cu(*R*,*R*)-Ph-box](OTf)$_2$-catalyzed aminooxygenation reaction set reported recently by Chemler *et al*. and summarized in eqs. 1 and 2. Development of a rigorous understanding of the enantioselectivity origin in the aminooxygenation reaction could more broadly impact the development of copper-catalyzed alkene difunctionalization reactions as the enantioselective carboamination, aminohalogenation, and hydroamination reactions summarized in eqs. 3-5, for example, are thought to occur via the same enantiodetermining aminocupration transition state (*vide infra*).

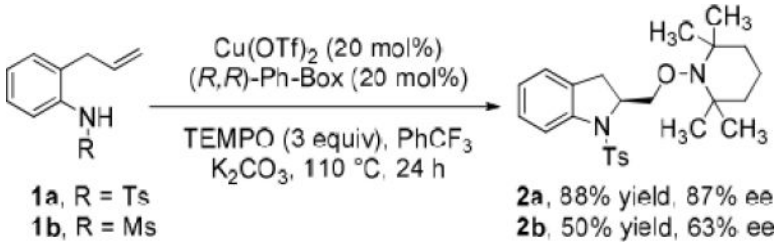

(1)

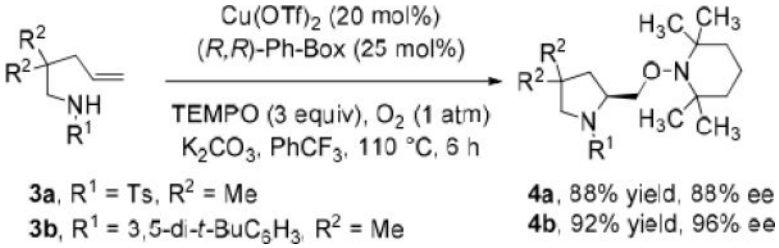

(2)

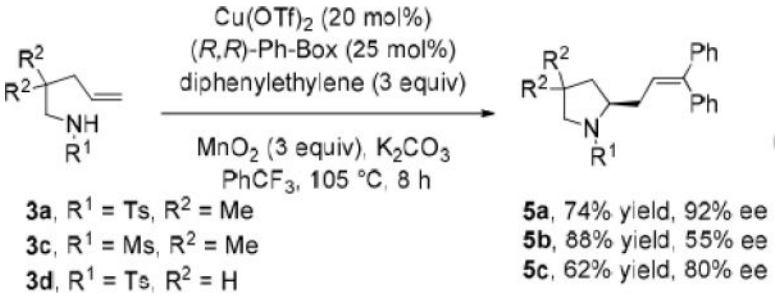

(3)

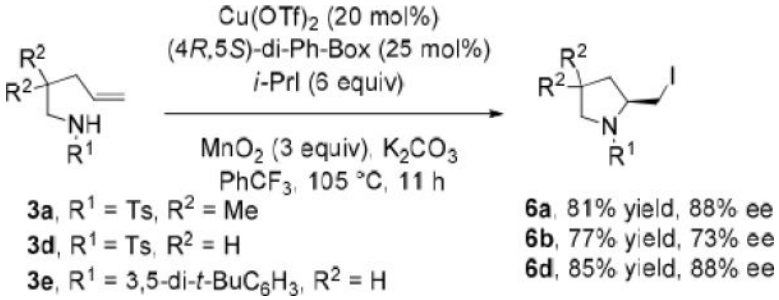

(4)

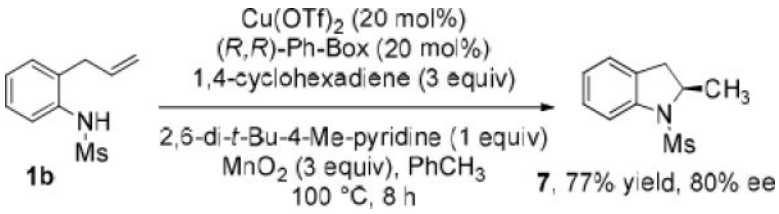

(5)

Catalytic Enantioselective Aminooxygenation

Recently we reported strong spectroscopic and kinetic evidence, as well as DFT calculations, which suggested that *cis*-aminocupration is the rate determining step in the copper(II) carboxylate-*promoted* intramolecular alkene aminooxygenation reaction (eq. 6).[18-20] Using H/D substituted alkenes, an inverse secondary kinetic isotope effect was observed in the alkene addition step (eq. 6), further supporting it as the rate-determining step. The reaction kinetics of the enantioselective copper-*catalyzed* aminooxygenation reaction (eq. 1) were also recently examined[21] and found to be first order in sulfonamide **1a**, first order in [Cu(*R*,*R*)-Ph-box](OTf)$_2$ and zero order in (2,2,6,6-tetramethylpiperidin-1-yl)oxyl (TEMPO). Additionally, using H/D substituted alkenes, an inverse secondary kinetic isotope effect was observed in the alkene addition step (eq. 7), indicating it is also as the rate-determining step in the catalytic reaction.

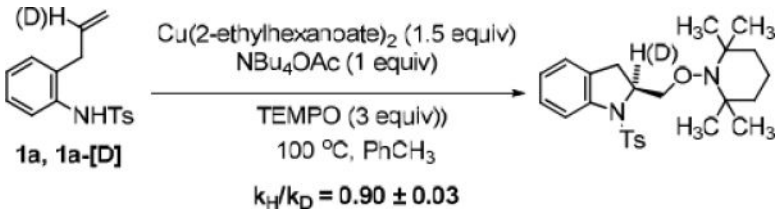

(6)

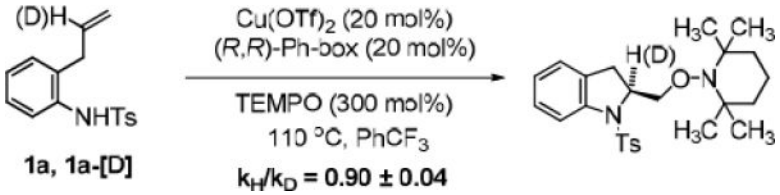

(7)

Based on the similarity of the copper-catalyzed and copper-promoted reactions, including similar diastereoselectivity trends,[18-20] we envisioned the proposed catalytic aminooxygenation reaction mechanism shown in Scheme 1. In this reaction, association of the amine nucleophile with the copper(II) center to form **8a** or **8b** is thought to be rapid, followed by rate-determining *cis*-aminocupration through a cyclic pro-(*S*) transition state (**TS-1S**). Loss of H^+ from the sulfonamide likely occurs after [Cu] association, when its pK_a would be lower. A base such as K_2CO_3 is usually necessary to sequester this proton (eqs. 1-5), but additional base was not necessary for the aminooxygenation reaction of **1a**. It is likely TEMPO anion (TEMPO is used in excess) serves as the base in this reaction. The resulting organocopper(II) intermediate, **9a** or **9b**, is unstable and undergoes C−Cu(II) bond homolysis to give Cu(I) and carbon radical **10**, followed by direct trapping of the carbon radical with TEMPO radical to provide the aminooxygenation product.[21] Reversible coordination of the triflate counterion for intermediates **8** and **9** reflects a mechanism refinement based upon the results of the calculations presented herein (*vide infra*). While Chemler and co-workers have proposed a working mechanistic hypothesis to rationalize formation of the major enantiomer (*e.g.*, pro-(*S*) **TS-1S**, Scheme 1),[7,21] no proposal of the competing pro-(*R*) transition state has been put forth. We report herein a detailed DFT study that provides energy-minimized models of the competing pro-(*S*) and pro-(*R*) transition states that shed light on the underlying factors that control this reaction's absolute stereochemistry.

METHODS

Calculations were carried out at the Kohn-Sham hybrid-DFT UB3LYP[22,23] level of theory using the Gaussian 09[24] and GaussView v5.0.8 programs. The GenECP method was employed with a 6-31G(d) basis set applied to all atoms (*i.e.*, H, C, N, O, F, S) except copper, which was computed using the Los Alamos LAN2DZ[25-28] basis set, as used in our theoretical study of the copper-promoted aminooxygenation reaction.[18] To account for the experimental use of polar solvents in this system, the Integral Equation Formalism Polarized Continuum Solvation Model (IEFPCM)[29] was used throughout the computations. Because the Gaussian 09 program does not contain default solvent parameters for the reaction

solvent, trifluorotoluene (ε = 9.18), those of 1,2-dichloroethane (ε = 10.13), which is supported by the program, and has a similar dielectric constant, were used instead.[30] The calculations were run at 383.15 K (110 °C) for consistency with experimental protocols. All transition states were confirmed to have only one imaginary frequency and the Intrinsic Reaction Coordinate (IRC) method[31] was used with default parameters followed by a geometry optimization to confirm the product species (minima, containing only real frequencies) resulting from the path of steepest descent for each transition state. To further support the computational data, single point energies were computed using the ωB97XD[32] functional in place of B3LYP for better representation of long range dispersion interactions, as well as at the ωB97XD/6-311G+(d,p)/SCRF=dichloroethane level of theory. Given the elevated temperatures at which the experiments were conducted, thermal energy corrections obtained from the optimized structures were included in all single point energies. This data can be found in the supporting information. Natural Bond Order (NBO) analysis was performed using Gaussian NBO Version 3.1.[33] The term 'tetrahedral twist angle' (θ_{TTA}) is used to define the angle between the plane containing the two nitrogen atoms of the bis(oxazoline) ligand ($N_{lig(1)}$ and $N_{lig(2)}$) and the copper atom, and the plane containing of the sulfonamide nitrogen (N_{sub}), the terminal carbon of the substrate's olefin (C_{sub1}), and the copper atom. To compute the θ_{TTA} the Mercury 2.4 program[34] TTA was used.

The reported ground states (*e.g.*, Figure 1 and Figure 2) were located using molecular mechanics based conformational distribution searches (MMFF94), which were performed using Spartan 04'.[35] In one conformational distribution search the coordinates of the copper atom, $N_{lig(1)}$, and $N_{lig(2)}$ were constrained. In another conformational distribution search the N_{sub} was also constrained. The five lowest energy conformers from each distribution search with observably different geometries were then re -optimized using Gaussian 09 at the abovementioned level of theory. The lowest energy minimum obtained from this procedure was chosen as the best approximation to the ground state complex.

Results and Discussion

Ground State Analysis—At the outset of this study we investigated the two ground state species resulting from coordination of [Cu(*R*,*R*)-Ph-box](OTf)$_2$ to *N*-tosyl-o-allyl aniline (**1a**) and *N*-tosyl-2,2-dimethylpent-4-en-1-amine (**3a**). While some copper(II) complexes are known to exhibit hexacoordinate, octahedral geometry,[36] copper(II) complexes with bis(oxazoline) ligands preferentially form four coordinate, square planar, and five-coordinate, square pyramidal species.[15,16,37] Interestingly, however, our calculations revealed that the most favorable substrate-catalyst ground state complex, [Cu(*R*,*R*)-Ph-Box(*N*-tosyl-*o*-allyl anilide)]$^{1+}$ (**8a**), was a three-coordinate species (Scheme 1 and Figure 1). Steric crowding around copper resulting from coordination of the substrate and ligand prevents a four-coordinate species that would result from further ligation of a sulfonamide oxygen atom, as seen with similar substrates in the presence of less sterically demanding copper complexes.[18] Moreover, this steric crowding prevents the direct ligation of a $^{-}$OTf ion, and the triflate ligand acts only as a counter-ion, residing outside the direct coordination sphere of the copper center. Consequently, to simplify our calculations the triflate counter-ion was omitted, and thus the modelled complexes have an overall +1 charge.

The copper center of [Cu(*R*,*R*)-Ph-Box(*N*-tosyl-*o* allyl anilide)]$^{1+}$ ground state (**8a**) possesses a distorted trigonal planar geometry. Making up the trigonal plane are the copper, $N_{lig(1)}$, $N_{lig(2)}$, and N_{sub} atoms. The sulfonamide oxygen resides above the trigonal plane, at a distance of 2.84 Å from the copper atom, in an apical position. NBO analysis revealed a correlation between the three N−Cu bond distances and their corresponding $N_{(LP)}\rightarrow Cu_{(LP^*)}$ donor-acceptor stabilization energies. Specifically, $N_{lig(1)}$ and $N_{lig(2)}$ show donor-acceptor energies (E_{NBO}) of 10.85 kcal/mol and 14.56 kcal/mol and have N−Cu bond distances of

2.05 Å, 2.02 Å, respectively, while the N_{sub}−Cu bond is 1.95 Å with an E_{NBO} of 24.73 kcal/mol. Given that Cu(II) has an unpaired electron, spin density analyses were performed in order to determine how the SOMO was distributed over the complex. It was found that 86.8% of the SOMO resides on Cu and the three nitrogen atoms with 22.4% on N_{sub}, 10.9% on the aniline ring, and 50.8% on copper.

The [Cu(*R*,*R*)-Ph-Box(*N* tosyl-2,2 dimethylpent-4-en-1-amide)]$^{1+}$ (**11a**) (Figure 2) shares many similarities with that of **8a**. Namely, the copper geometry in **11a** is also distorted trigonal planar, and a similar relationship was observed between the three N-Cu bond distances and their corresponding $N_{(LP)}\rightarrow Cu_{(LP^*)}$ donor-acceptor stabilization energies. Specifically, the $N_{lig(1)}$−Cu and $N_{lig(2)}$−Cu bond distances were 2.02 Å and 2.00 Å, with NBO donor-acceptor energies of 14.15 kcal/mol and 17.01 kcal/mol, respectively, while the N_{sub}–Cu distance is 1.91 Å with an E_{NBO} of 24.73 kcal/mol. Furthermore, the sulfonamide oxygen of **11a** occupies an apical coordination site with respect to the copper atom, at a distance of 2.83 Å, with an E_{NBO} of 3.04 kcal/mol, consistent with **8a**, however in contrast to ground state **8a**, the lack of an aniline ring system in **11a** resulted in delocalization of the SOMO almost entirely onto Cu and the three N-atoms (94%), with 30% of the spin density on N_{sub} and 49% on copper.

Transition State Analysis—From ground state **8a** the lowest energy pro-(*S*) and pro-(*R*) transition states (Figure 3) for the *N*-tosyl-*o*-allyl aniline substrate **1a** were calculated (**TS-1S** and **TS-1R**, respectively). The pro-(*S*) mode of addition, via **TS-1S**, was favored by $\Delta\Delta G^{\ddagger}$ = 1.5 kcal/mol (calculated ee = 75%), which is qualitatively consistent with experimental observations (eq. 1, *vide supra*). A notable feature of these two transition states is how the coordination geometry of copper differs between the two stereofacial modes of addition. **TS-1S** has a tetrahedral twist angle (θ_{TTA}) of 26.25 °, and thus a distorted square planar geometry, while **TS-1R** has a θ_{TTA} of 50.45 ° and hence a distorted tetrahedral geometry.[38] Spin density analysis of **TS-1S** revealed 26.8% spin on C_{sub1} accompanied by a 7.5 % decrease in spin density on Cu and a 6.8 % decrease in spin on N_{sub}, relative to ground state **8a**. Since the majority of the spin still resides on Cu, it is likely that the SOMO is simply delocalized onto the coordinated atoms, while the $(N\text{-}C)_{sub}$ bond formation itself possesses a noticeable level of charge separation, as supported by the change in Mulliken charges on going from the ground state to **TS-1S** (Mulliken charges **8a**: N_{sub} (−0.795), C_{sub1} (−0.369), and **TS-1S**: N_{sub} (−0.757), C_{sub1} (−0.467))

Placed in the context of the steric environment created by the C_2-symmetric nature of the metal-ligand complex, and the simple pneumonic depiction for stereoinduction in Figure 4b, the *N*-substituent is confined to two of the four existing quadrants. The specific quadrants to which the *N*-substituent is confined differ between the two stereofacial modes of addition. For the case at hand, it is observed that in the pro-(*R*) mode of addition the *N*-substituent can reside only in quadrant QII or QIII, while in the pro-(*S*) addition mode the *N*-substituent lies either in quadrant QI or QIV. As such, the pro-(*R*) transition states, as opposed to the pro-(*S*) transition states, suffer from more unfavourable van der Waals contacts between the *N*-substituent and the phenyl group of the Ph box ligand.

Entailed with this picture is the concept of the tetrahedral twist metric (θ_{TTA}), which as noted above is the distortion from an ideal planar geometry about copper. As can be seen from this model, to alleviate repulsive steric contacts the pro-(*R*) series of transition states adopt a larger θ_{TTA}, resulting in poorer orbital overlap and an increase in $\Delta\Delta G^{\ddagger}$, rendering the reaction selective for pro-(*S*). It thus appears that optimal orbital alignment in this system occurs when the copper's d-orbitals are co-planar with the π-bond of the olefin, and the lone pairs of N_{sub} (Figure 4a). This is evidenced by the resulting differences in NBO stabilization energies, bond distances, and overall free energies of activation (summarized in Table 1,

vide infra). However, the large d-orbitals of Cu can tolerate significant deviation from planarity.

We next examined the aminocupration of *N*-tosyl-2,2-dimethylpent-4-en-1-amine, **3a** (*vide supra*, eq. 2), for which the lowest energy pro-(*S*) and pro-(*R*) transition states (**TS-2S** and **TS-2R** respectively) are shown in Figure 5a and 5b. Again, a change in coordination geometry is observed between the two stereofacial transition states (**TS-2S** θ_{TTA} = 13.38°, **TS-2R** θ_{TTA} = 44.21°), rendering **TS-2S** lower in energy by $\Delta\Delta G^{\ddagger}$ = 2.7 kcal/mol, equating to a calculated ee of 93.4%. However, in this aliphatic substrate, an interesting trend not applicable to the aromatic substrate is observed, wherein the substrate adopts a 7-membered ring-type, chair or boat conformation, depending on the stereofacial mode of addition.[39,40] Specifically, **TS-2S** takes on a chair conformation, while **TS-2R** takes on a boat conformation. The reason for this can be rationalized within the context of the quadrant model. In **TS-2S** the tosyl group sits in an empty quadrant, while in **TS-2R**, it lies in an occupied quadrant, generating unfavourable van der Waals contacts with the phenyl group of the Ph-box ligand. When the substrate backbone takes on a chair conformation, the geminal dimethyl unit forces the tosyl group further into this unfavourable quadrant, magnifying the steric effect. Thus, the substrate adopts a boat-type transition state to help alleviate steric repulsion.

The NBO energies and bond forming and breaking distances for competing transition states **TS-1S** and **TS-1R** as well as **TS-2S** and **TS-2R** are summarized in Table 1. The comparative NBO energies indicate that the distorted square planar geometries provide greater stabilization (Table 1). In the *N*-tosyl-*o*-allyl aniline series, donation of the alkene double bond (C_{sub1}–C_{sub2}) into copper is 2.96 kcal/mol greater in **TS-1S** than in **TS-1R**. Additionally, lone pair donation of N_{sub} into the alkene double bond is 5.04 kcal/mol greater in **TS-1S** than in **TS-1R.** As a result, **TS-1S** has a shorter $(N–C)_{sub}$ bond forming distance, a shorter C_{sub1}–Cu interatomic distance, and a longer N_{sub}–Cu distance. Taken together, these bond distances and corresponding NBO donor acceptor energies suggest that $(N–C)_{sub}$ and C_{sub1}–Cu bond making, and N_{sub}–Cu bond breaking are more developed within **TS-1S** than **TS-1R**. This is further exemplified by the lower Mulliken charge on N_{sub} (**TS-1S** = 0.757, **TS-1R** = -0.780, Figures 3a and 3b) and the higher charge on the terminal CH_2 carbon of the olefin (**TS-1S** = -0.476, **TS-1R** = -0.466, Figure 4a and 4b), signifying that in **TS-1S** the negative charge on nitrogen is being donated into the olefin to a larger extent. Analysis of the spin density within **TS-2S** revealed the presence of 24.7% spin on C_{sub1} accompanied by a 6.0 % decrease in spin density on Cu and a 15.8 % decrease in spin on N_{sub}, relative to ground state **11a**. Similar to **TS-1S**, the bulk of the spin density still resides on Cu, with the SOMO delocalized onto the coordinated atoms. Moreover, $(N\text{-}C)_{sub}$ bond formation shares a degree of charge separation, as supported by the change in Mulliken charges on going from the ground state to **TS-2S** (Mulliken charges **11a**: N_{sub} (−0.695), C_{sub1} (−0.387), and **TS-2S**: N_{sub} (−0.670), C_{sub1} (−0.480)).

Interestingly, irrespective of whether the transition states **TS-2S** and **TS-2R** for the aliphatic substrate **3a** adopts a chair-like or a boat-like geometry, the $(N–C)_{sub}$ bond forming distances, and their respective NBO $N_{LP} \rightarrow \pi^*_{C=C}$ donor acceptor energies remain similar (Table 1). On the other hand, the C_{sub1}–Cu bond is comparatively shorter in **TS-2S**, and has a much greater donor – acceptor stabilization energy (Table 1). Consistent with the previous substrate, this data suggests that **TS-2S** is more developed than **TS-2R**. Furthermore, the elongated N_{sub}–Cu bond distance in **TS-2S**, compared with **TS-2R** (Table 1), is accompanied by a larger shift in charge density to the terminal alkene carbon (C_{sub1}), as witnessed by an increase in the computed Mulliken charges (Figures 5a and 5b). As summarized in Table 1, both pro-(*S*) transition states have lower distortion from planarity than the corresponding pro-(*R*) transition states (lower θ_{TTA}).

Further analysis of the interatomic distances in **TS-1S** and **TS-2S** (Table 1) reveals C_{sub1}-Cu bond forming distances of 2.12 Å and 2.13 Å, and $(N\ C)_{sub}$ bond forming distances of 2.05 Å and 2.09 Å. In comparison, the final C_{sub1}-Cu bond distances in the local minima **12** and **13** (Scheme 2, *vide infra*) were both found to be 1.98 Å, while the final $(N\text{-}C)_{sub}$ bond distances were 1.53 Å and 1.52 Å. Taken together, this suggests that C_{sub1}-Cu bond formation is significantly more developed at the transition state than $(N\text{-}C)_{sub}$ bond formation, indicating C_{sub1}-Cu bond formation precedes that of $(N\text{-}C)_{sub}$ bond formation in a concerted, asynchronous manner, consistent with previous results.[18]

Rationalizing Observed Selectivity Trends Based on Substrate Structure

Experimentally, it is observed that smaller sulfonamide R groups on the substrate give lower levels of enantioselectivity in the reaction (*vide supra*, eqs. 1-5). For example, aryl sulfonamides provide higher selectivity than methyl (*e.g.*, Ts vs. Ms), and even higher enantioselectivity is observed with substrates bearing the 3,5-di-*tert*-butylbenzenesulfonamide group (eqs. 2 and 4). This is seen as a general trend for the synthesis of indolines and pyrrolidines via the copper-catalyzed aminooxygenation, aminohalogenation, and carboamination (eqs. 1-4). It is also observed experimentally that 4-pentenylsulfonamides with 2,2-gem-dialkyl or 2,2-gem-diaryl backbone substitution react with higher enantioselectivity than the parent 4-pentenylsulfonamides (eqs. 3 and 4).

To discern the origin of these observations, the effects of *N*-substitution on selectivity were investigated by DFT. Having already considered the *N*-tosyl substrate, our attention turned to an analysis of *N*-3,5-di-*tert*-butylbenzenesulfonamide, **3b**, and the *N*-mesyl substrate **3c**. Most importantly, the relative energetic preferences calculated for the pro-(*S*) transition states for substrates **3a**-**3c** were qualitatively consistent with the experimentally observed enantioselectivity (*vide supra*, eqs. 2-4, **3a** = 94% *ee* (2.7 kcal/mol), **3b** = 96% *ee* (3.0 kcal/mol), and **3c** = 86% *ee* (2.0 kcal/mol)). The pro-(*S*) and pro-(*R*) transition states of **3b** and **3c** shared a number of key features with those of **3a**. Namely, the calculated pro-(*S*) transition states (**TS-3S** and **TS-4S**) possessed distorted square planar geometries (Table 2) wherein the substrate backbones adopted chair-like conformations. Comparatively, the pro-(*R*) transition states (**TS-3R** and **TS-4R**) possessed distorted-tetrahedral geometries and adopted boat-like conformations. What is more, the computed inter-atomic distances and Mulliken charges (Tables 2 and 3) indicate that the pro-(*S*) transition states are more developed than the pro-(*R*) transition states. Specifically, the $(N\text{-}C)_{sub}$ and C_{sub1}-Cu bond forming distances in **TS-3S** and **TS-4S** were slightly shorter than in **TS-3R** and **TS-4R** and the N_{sub}-Cu bond breaking distances were noticeably longer. As well, the pro-(*S*) transition states displayed larger Mulliken charges on copper and the internal olefinic carbon. In terms of the observed differences in enantioselectivity, the increased preference for the pro-(*S*) transition states over the pro-(*R*) transition states in the case of **3a** and **3b** is attributed to the greater ability of the pro-(*S*) transition states to accommodate steric bulk on R1, on account of the quadrant model. Additionally, the pro-(*S*) transition states are further stabilized by the presence of a C-H•••π interaction between the substrate's R2 methyl group and its R1 aryl group (R's refer to equation 2). The existence of this interaction was supported by an AIM analysis which revealed the presence of a bond critical point (BCP) between a hydrogen of the R2 methyl group and the π-system of the R1 aryl ring (see Supporting Information). Moreover, when R1 = Ms, not only is this stabilizing interaction not present, but it is instead replaced by a repulsive interaction, thus decreasing the energetic preference of **TS-4S** over **TS-4R**.

To investigate the effect of the gem-dimethyl group of the substrate on reaction selectivity, 3,5-di-*tert*-butylbenzenesulfonamide of pent-4-en-1-amine, **3e**, which lacks a gem-dimethyl group, was considered. Experimentally, substrates that lack geminal dialkyl or diaryl substitution (*e.g.*, **3d** and **3e**) give about 10% lower enantioselectivity than substrates with

geminal di-substitution (*e.g.*, **3a** and **3b**, *e.g.*, eqs. 3 and 4). The computed transition states for **3e** also showed a lower level of selectivity compared to **3b** (computed ee = 93 % vs. 96 %). The origin of this decrease in selectivity is attributed in part to a greater range of motion of the *N*-tosyl substituent which in turn allows it to move away from the occupied quadrant, and a less favourable C-H•••π interaction in chair-type transition state of **3e** (**TS-5S**), compared with that of **3b** (**TS-4S**). In **TS-4S** the distance between the methyl C-H and the nearest carbon of the aryl ring is 2.77 Å, possessing a BCP ρ_b of 0.0068, while in **TS-5S** the distance between the methylene C-H and the nearest carbon of the aryl ring is 3.01 Å, and the BCP ρ_b is 0.0050.

With an understanding of the underlying factors governing the stereodetermining, Cu-mediated, C−N bond formation our interest turned to the overall reaction pathway. The complete mechanisms for the enantioselective copper-catalyzed aminooxygenations of substrates **1a** and **3a** are shown in Scheme 2. The reaction coordinates for the aminooxygenation of *N*-tosyl-2,2-dimethylpentenamine **3a** (Pathway A) and *N*-tosyl-*o*-allyl aniline **1a** (Pathway B) are shown in Figure 9 (coordinates and thermochemical data for all calculated transition states and intermediates can be found in the Supporting Information).

The ground state energies for pathways **A** and **B** were both arbitrarily set to 0.0 kcal/mol in order to draw comparisons from their relative energetic trends. The rate-limiting aminocupration step is $\Delta G^{\ddagger}$ = 19.4 kcal/mol for pathway **A** and $\Delta G^{\ddagger}$ = 18.2 kcal/mol for pathway **B**. In practice, the *N*-tosyl-*o*-allylaniline derived substrate **1a** is more reactive than the 4-pentenylsulfonamide **3a**, in agreement with the calculated relative energies. The first calculated intermediates to emerge from the aminocupration step are the organocopper intermediates **12** and **13**, where the sulfonamide nitrogens are still coordinated to the copper. Rotation about the resulting Cu—C bond eliminates N···Cu coordination, providing **14** and **9a**, respectively. This step is slightly endothermic in path **A** and slightly exothermic in path **B**, perhaps reflecting the relative basicities of the two nitrogens. Intermediates **14** and **9a** are charge separated tri-coordinate copper(I) complexes where the triflate resides in the outer sphere. Covalent attachment of the triflate to the copper center resulted in higher energy intermediates. Energetically favourable C—Cu homolysis then ensues, providing the primary alkyl radicals **15** and **10** and [Cu(*R*,*R*)-Ph-box]OTf, a Cu(I) species. The alkyl radicals are then trapped by TEMPO, providing the aminooxygenation products (Pathway **A**: ΔG_{rxn} = −20.8 kcal/mol, pathway **B**: ΔG_{rxn} = −16.0 kcal/mol).

CONCLUSION

In summary we have presented a rationale accounting for the enantioselectivity of the [Cu(*R*,*R*)-Ph-box](OTf)$_2$ catalyzed intramolecular aminooxygenation of γ-unsaturated sulfonamides using Density Functional Theory. The stereochemical preference of the pro-(*S*) transition states is the interplay between optimal orbital overlap, quadrant-based steric repulsion, and the tetrahedral twist angle (θ_{TTA}). In particular, we have found that for the substrates investigated herein, the favored, pro-(*S*) transition states contain copper(II) centers with distorted square planar geometry while the minor, pro-(*R*) transition states contain copper(II) centers with geometry more consistent with distorted tetrahedral. Measurements of bond lengths, E_{NBO}, and Mulliken charges indicate that those transition states having square planar copper(II) geometry are more developed, as a result of better orbital overlap. In addition, a conformational trend for the pro-(*S*) and pro-(*R*) transition states of the *N*-(4-pentenyl)sulfonamides examined emerged; the major, pro-(*S*) transition states adopted chair-like, seven-membered cyclization conformations, while the minor, pro-(*R*) transition states adopted boat-like, seven-membered cyclization conformations. Both the change in geometry about copper(II) and the change in cyclization conformation appeared to be the result of minimization of steric interactions between the substrate's *N*-sulfonyl group

and the phenyl substituent of the bis(oxazoline) ligand in the pro-(*R*) transitions states, as per the quadrant model. Thus, the substrate's *N*-sulfonyl group plays a significant role in the reaction's enantioselectivity, which was further observed by changes in selectivity with changes in the *N*-sulfonyl group. The pro-(*S*) and pro-(*R*) transition states described in this paper are similar to those proposed for other metal-catalyzed enantioselective *cis*-aminometallation/cyclization transitions states (*e.g.*, hydroamination with lanthanides)[41] in that a seven-membered chair-like conformation is invoked for the major transition state, but to our knowledge, this is the first time a boat-like conformation is invoked to rationalized product formation through the minor transition state. The sterically demanding sulfonamide moiety in our substrates makes alternative, minor chair-like transition states more energetically demanding. The results described in this report should aid in the more complete understanding and further design of the growing body of alkene difunctionalization reactions catalyzed by [Cu(*R*,*R*)-Ph-box](OTf)$_2$ and related catalysts.[6-14]

Supplementary Material

Refer to Web version on PubMed Central for supplementary material.

Acknowledgments

Financial support for this work was provided by the National Institutes of Health, NIGMS (GM-078383) and L.B. is the recipient of a Queen Elizabeth II Scholarship. We thank Dr. Yan Miller for helpful suggestions and SHARCNET[42] for computing resources.

REFERENCES

1. Chemler SR. Org. Biomol. Chem. 2009; 7:3009–3019. [PubMed: 20976023]
2. McDonald RI, Liu G, Stahl SS. Chem. Rev. 2011; 111:2981–3019. [PubMed: 21428440]
3. Zaitsev AB, Adolfsson H. Synthesis. 2006:1725–1756.
4. De Jong S, Nosal DG, Wardrop DJ. Tetrahedron. 2012; 68:4067–4105. [PubMed: 22888177]
5. Donohoe TJ, Callens CKA, Lacy AR, Winter C. Eur. J. Org. Chem. 2012:655–663.
6. Zeng W, Chemler SR. J. Am. Chem. Soc. 2007; 129:12948–12949. [PubMed: 17918850]
7. Fuller PH, Kim J-W, Chemler SR. J. Am. Chem. Soc. 2008; 130:17638–17639. [PubMed: 19049311]
8. Sequiera FC, Turnpenny BW, Chemler SR. Angew. Chem. Int. Ed. 2010; 49:6365–6368.
9. Miao L, Haque I, Manzoni MR, Tham WS, Chemler SR. Org. Lett. 2010; 12:4739–4741. [PubMed: 20873817]
10. Liwosz TW, Chemler SR. J. Am. Chem. Soc. 2012; 134:2020–2023. [PubMed: 22257169]
11. Bovino MT, Chemler SR. Angew. Chem. Int. Ed. 2012; 51:3923–3927.
12. Miller Y, Miao L, Chemler SR. J. Am. Chem. Soc. 2012; 134:12140–12156.
13. Turnpenny BW, Hyman KL, Chemler SR. Organomet. 2012; 31:7819–7822.
14. Sanjaya S, Chiba S. Org. Lett. 2012; 14:5342–5345. [PubMed: 23030596]
15. Desimoni G, Falta G, Jorgensen KA. Chem. Rev. 2006; 106:3561–3651. [PubMed: 16967916]
16. Johnson JS, Evans DA. Acc. Chem. Res. 2000; 33:325–335. [PubMed: 10891050]
17. Rasappan R, Laventine D, Reiser O. Coord. Chem. Rev. 2008; 252:702–714.
18. Paderes MC, Belding L, Fanovic B, Keister JB, Dudding T, Chemler SR. Chem.—Eur. J. 2012; 18:1711–1726. [PubMed: 22237868]
19. Paderes MC, Chemler SR. Org. Lett. 2007; 9:2745–2758. [PubMed: 17559222]
20. Paderes MC, Chemler SR. Eur. J. Org. Chem. 2011:3679–3684.
21. Paderes MC, Keister JB, Chemler SR. J. Org. Chem. 2013; 78:506–515. [PubMed: 23244027]
22. Becke AD. J. Chem. Phys. 1993; 98:5648–5652.
23. Lee C, Yang W, Parr RG. Phys. Rev. B. 1988; 37:785–789.

24. Frisch, MJ.; Trucks, GW.; Schlegel, HB.; Scuseria, GE.; Robb, MA.; Cheeseman, JR.; Scalmani, G.; Barone, V.; Mennucci, B.; Petersson, GA.; Nakatsuji, H.; Caricato, M.; Li, X.; Hratchian, HP.; Izmaylov, AF.; Bloino, J.; Zheng, G.; Sonnenberg, JL.; Hada, M.; Ehara, M.; Toyota, K.; Fukuda, R.; Hasegawa, J.; Ishida, M.; Nakajima, T.; Honda, Y.; Kitao, O.; Nakai, H.; Vreven, T.; Montgomery, JA., Jr.; Peralta, JE.; Ogliaro, F.; Bearpark, M.; Heyd, JJ.; Brothers, E.; Kudin, KN.; Staroverov, VN.; Kobayashi, R.; Normand, J.; Raghavachari, K.; Rendell, A.; Burant, JC.; Iyengar, SS.; Tomasi, J.; Cossi, M.; Rega, N.; Millam, JM.; Klene, M.; Knox, JE.; Cross, JB.; Bakken, V.; Adamo, C.; Jaramillo, J.; Gomperts, R.; Stratmann, RE.; Yazyev, O.; Austin, AJ.; Cammi, R.; Pomelli, C.; Ochterski, JW.; Martin, RL.; Morokuma, K.; Zakrzewski, VG.; Voth, GA.; Salvador, P.; Dannenberg, JJ.; Dapprich, S.; Daniels, AD.; Farkas, Ö .; Foresman, JB.; Ortiz, JV.; Cioslowski, J.; Fox, DJ. Gaussian, Inc.; Wallingford CT: 2009. Gaussian 09, Revision C.01
25. Dunning, THJ.; Hay, PJ. Methods of Electronic Structure Theory (Modern Theoretical Chemistry). Schaefer, HF., III, editor. Plenum; New York: 1977. p. 1-28.
26. Hay PJ, Wadt WR. J. Chem. Phys. 1985; 82:270–283.
27. Hay PJ, Wadt WR. J. Chem. Phys. 1985; 82:299–310.
28. Wadt WR, Hay PJ. J. Chem. Phys. 1985; 82:284–298.
29. Tomasi J, Mennucci B, Cance E. J. Mol. Struc. (Theochem). 1999; 464:211–226.
30. Although DCM has been used to represent TFT due to its higher similarity in dielectric constant, (*Org. Lett.* **2009**, *11*, 37-40.) the size of solvent cavity of DCE was deemed to be closer to TFT with a sufficiently similar dielectric constant
31. Fukui K. Acc. Chem. Res. 1981; 14:363–368.
32. Chai JD, Head-Gordon M. Phys. Chem. Chem. Phys. 2008; 10:6615–6620. [PubMed: 18989472]
33. Glendening, ED.; Reed, AE.; Carpenter, JE.; Weinhold, F. NBO Version 3.1
34. Macrae CF, Bruno IJ, Chisholm JA, Edgington PR, McCabe P, Pidcock E, Rodriguez-Monge L, Taylor R, van de Streek J, Wood PA. J. Appl. Cryst. 2008; 41:466–470.
35. Hehre, WJ. Wavefunction; Irvine: 2003.
36. Persson I, Persson P, Sandström M, Ullström A-S. J. Chem. Soc, Dalton Trans. 2002:1256–1265.
37. Thorhauge J, Robertson M, Hazell RG, Jorgensen KA. Chem.—Eur. J. 2002; 8:1888–1898. [PubMed: 12007099]
38. Paschke R, Liebsch S, Tschierske C, Oakley MA, Sinn E. Inorg. Chem. 2003; 42:8230–8240. [PubMed: 14658873]
39. Bocian DF, Pickett HM, Rounds TC, Strauss HL. J. Am. Chem. Soc. 1975; 97:687–695.
40. Yeh PL, Tai CK, Shih TL, Hsiao HL, Wang BC. J. Mol. Struct. 2012; 1018:64–71.
41. Hong S, Tian S, Metz MV, Marks TJ. J. Am. Chem. Soc. 2003; 125:14768–14783. [PubMed: 14640652]
42. http://www.sharcnet.ca.

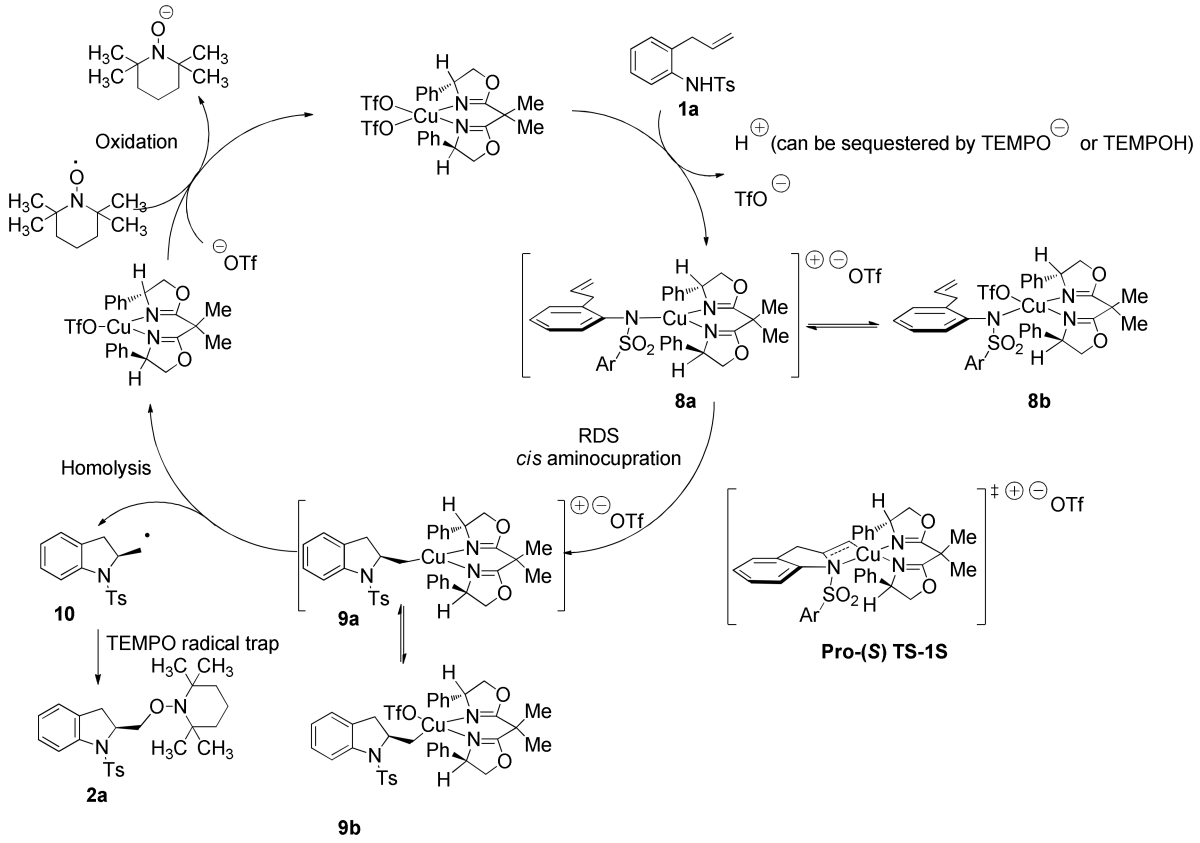

Scheme 1.
Proposed Copper Catalyzed Enantioselective Aminooxygenation Cycle

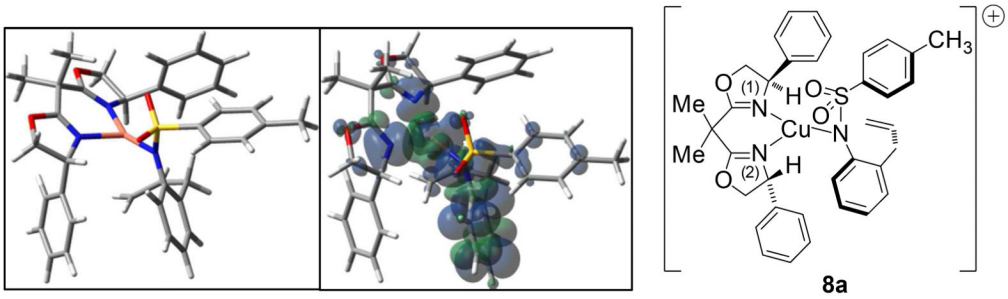

Figure 1.

Calculated ground state complex **8a** ([Cu(*R*,*R*)-Ph-Box(*N*-tosyl-*o*-allyl anilide)]$^{1+}$), resulting from coordination of sulfonamide **1a** to[Cu(*R*,*R*)-Ph-box](OTf)$_2$.

(i) Spin Densities: Cu (50.8%), N_{sub} (22.4%), $N_{lig(1)}$ (8.8%), $N_{lig(2)}$ (4.8%), Ar_{sub} 10.9%; (ii) Bond Distances: $O_{sulfony}$ –Cu (2.84 Å), N_{sub}–Cu (1.95 Å), $N_{lig(1)}$ –Cu (2.02 Å), $N_{lig(2)}$–Cu (2.05 Å); (iii) Mulliken Charges: $N_{lig(1)}$ (−0.514), $N_{lig(2)}$ (−0.503), Cu (0.602), N_{sub} (−0.795), C_{sub1} (−0.369), C_{sub2} (−0.066), and S (1.328).

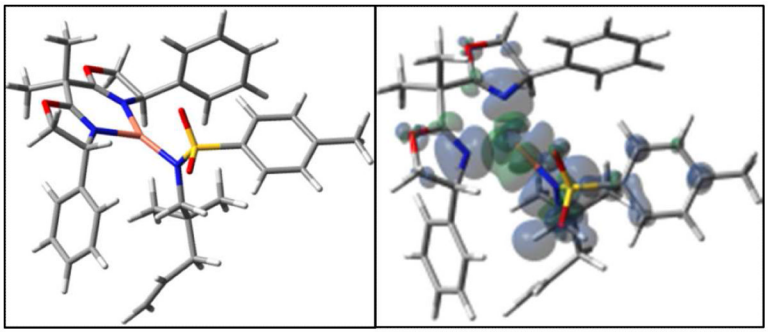

Figure 2.

Calculated ground state complex **11a** ([Cu(*R*,*R*)-Ph-Box(*N*-tosyl-2,2 dimethylpent-4-en-1-amide)]$^{1+}$), resulting from coordination of sulfonamide **3a** to[Cu(*R*,*R*)-Ph-box](OTf)$_2$. (i) Spin Densities: Cu (49.1%), $N_{lig(1)}$ (5.1%), $N_{lig(2)}$ (8.2%), N_{sub} (32.2%); (ii) Bond Distances: $O_{sulfonyl}$–Cu (2.83 Å), N_{sub}–Cu (1.91 Å), $N_{lig(1)}$–Cu (2.00 Å), $N_{lig(2)}$–Cu (2.02 Å); (iii) Mulliken Charges: $N_{lig(1)}$ (−0.522), $N_{lig(2)}$ (−0.521), Cu (0.604), N_{sub} (−0.695), C_{sub1} (−0.387), C_{sub2} (−0.070), and S (1.310).

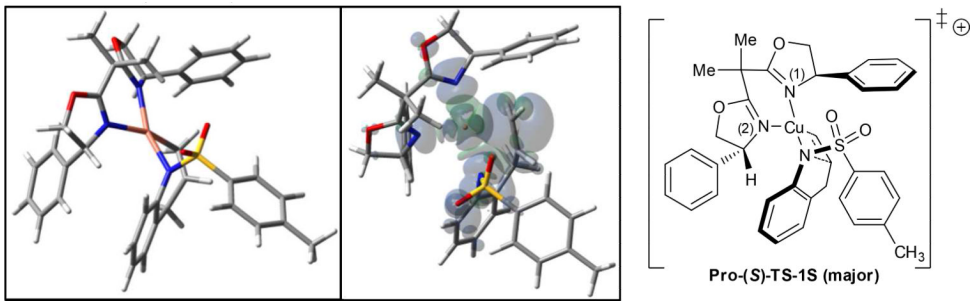

Figure 3a.

Computed *N*-tosyl-*o*-allyl aniline pro-(*S*) $(N–C)_{sub}$ bond forming transition state structure (**TS-1S**).

(i) Mulliken Charges: $N_{lig(1)}$ (−0.468), $N_{lig(2)}$ (−0.475), Cu (0.429), N_{sub} (−0.757), C_{sub1} (−0.476), C_{sub2} (0.051), and S (1.307); (ii) Spin Densities: Cu (43.3%), N_{sub} (15.6%), C_{sub1} (26.8%), $N_{lig(1)}$ and $N_{lig(2)}$ (9.7%).

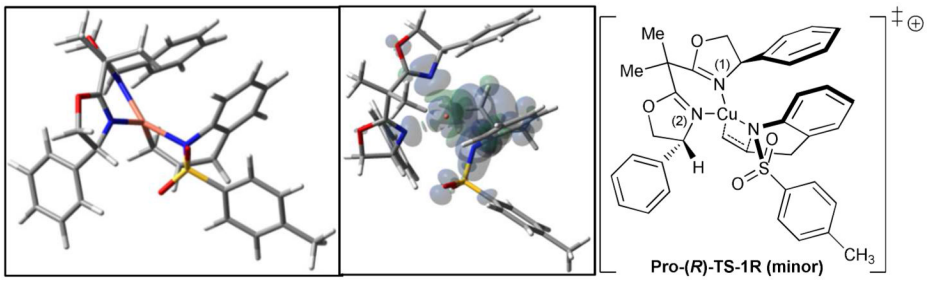

Figure 3b.

Computed *N*-tosyl-*o*-allyl aniline pro-(*R*) $(N–C)_{sub}$ bond forming transition state structure (**TS-1R**).

(i) Mulliken Charges: $N_{lig(1)}$ (−0.476), $N_{lig(2)}$ (−0.461), Cu (0.431), N_{sub} (−0.780), C_{sub1} (−0.466), C_{sub2} (0.051), and S (1.302); (ii) Spin Densities: Cu (43.1%), N_{sub} (15.8%), C_{sub1} (27.3%), $N_{lig(1)}$ and $N_{lig(2)}$ (7.7%).

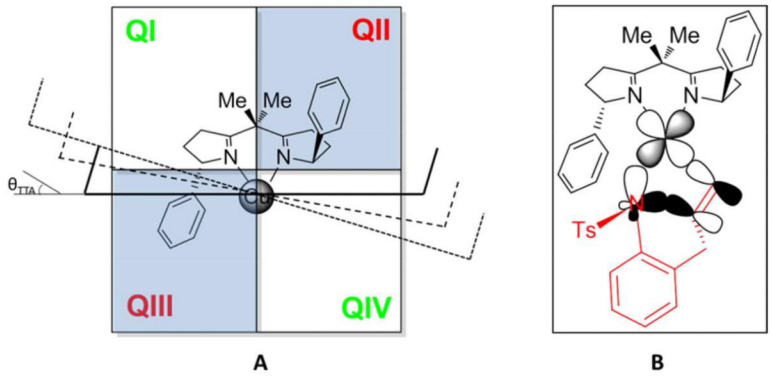

Figure 4.

(a) Graphic representation the tetrahedral twist angle and the quadrant model of steric induction; **(b)** Pictorial representation of the orbital alignment for $(N\text{-}C)_{sub}$ bond formation in **TS-1S**.

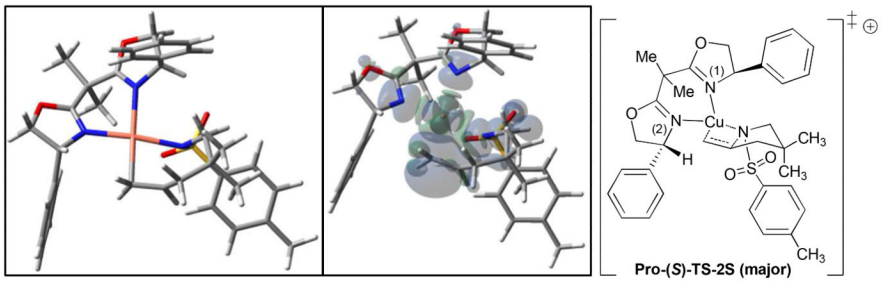

Figure 5a.

N-tosyl-2,2-dimethylpent-4-en-1-amine pro-(*S*) **TS-2S**.

(i) Mulliken Charges: $N_{lig(1)}$ (−0.467), $N_{lig(2)}$ (−0.468), Cu (0.392), N_{sub} (−0.670), C_{sub1} (−0.480), C_{sub2} (0.076), and S (1.304); (ii) Spin Densities: Cu (43.1%), N_{sub} (16.4%), C_{sub1} (24.7%), $N_{lig(1)}$ and $N_{lig(2)}$ (10%).

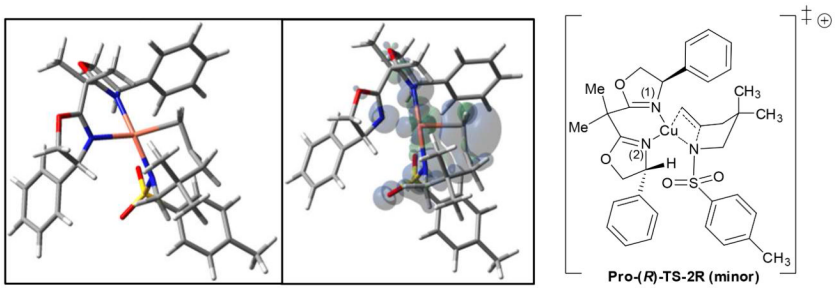

Figure 5b.

N-tosyl-2,2-dimethylpent-4-en-1 amine pro-(*R*) **TS-2R**.

(i) Mulliken Charges: $N_{lig(1)}$ (−0.467), $N_{lig(2)}$ (−0.461), Cu (0.318), N_{sub} (−0.668), C_{sub1} (−0.448), C_{sub2} (0.046), and S (1.307); (ii) Spin Densities: Cu (39.9%), N_{sub} (17.6%), C_{sub1} (31.2%), $N_{lig(1)}$ and $N_{lig(2)}$ (7.6%).

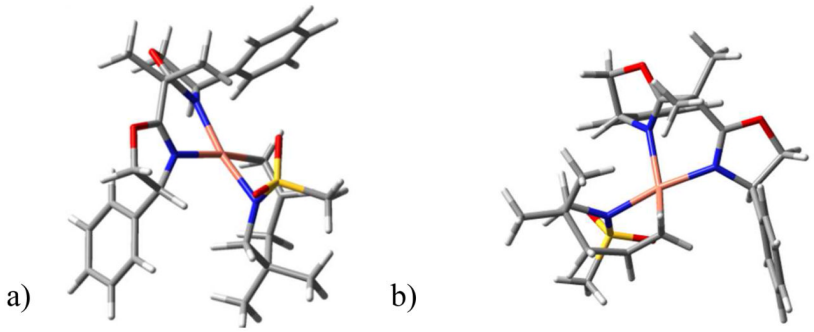

Figure 6.
(a) *N*-mesyl-2,2-dimethylpent-4-en-1-amine (**3c**) pro-(*S*): **TS-3S** (Major, Chair like); (b) *N*-mesyl-2,2-dimethylpent-4-en-1-amine (**3c**) pro-(*R*): **TS-3R** (Minor, boat-like).

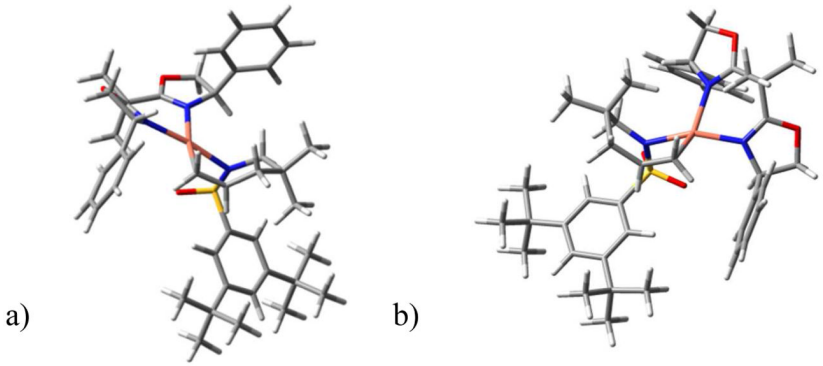

Figure 7.
(a) *N*-di-*tert*-butylphenylsulfonyl (**3b**) pro-(*S*): **TS-4S** (Major, Chair-like); (b) *N*-di-*tert*-butylphenylsulfonyl (**3b**) pro-(*R*): **TS-4R** (Minor, Boat-like).

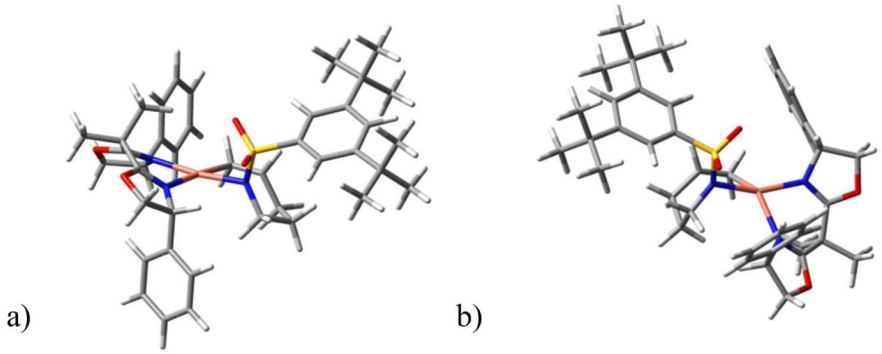

Figure 8.
(a) *N*-(di-*tert*-butylphenylsulfonyl)-pent-4-en-1-amine (**3e**) pro-(*S*): **TS-5S** (Major, Chair-like); (b) *N*-(di *tert*-butylphenylsulfonyl)-pent-4-en-1-amine (**3e**) pro-(*R*): **TS-5R** (Minor, Boat-like).

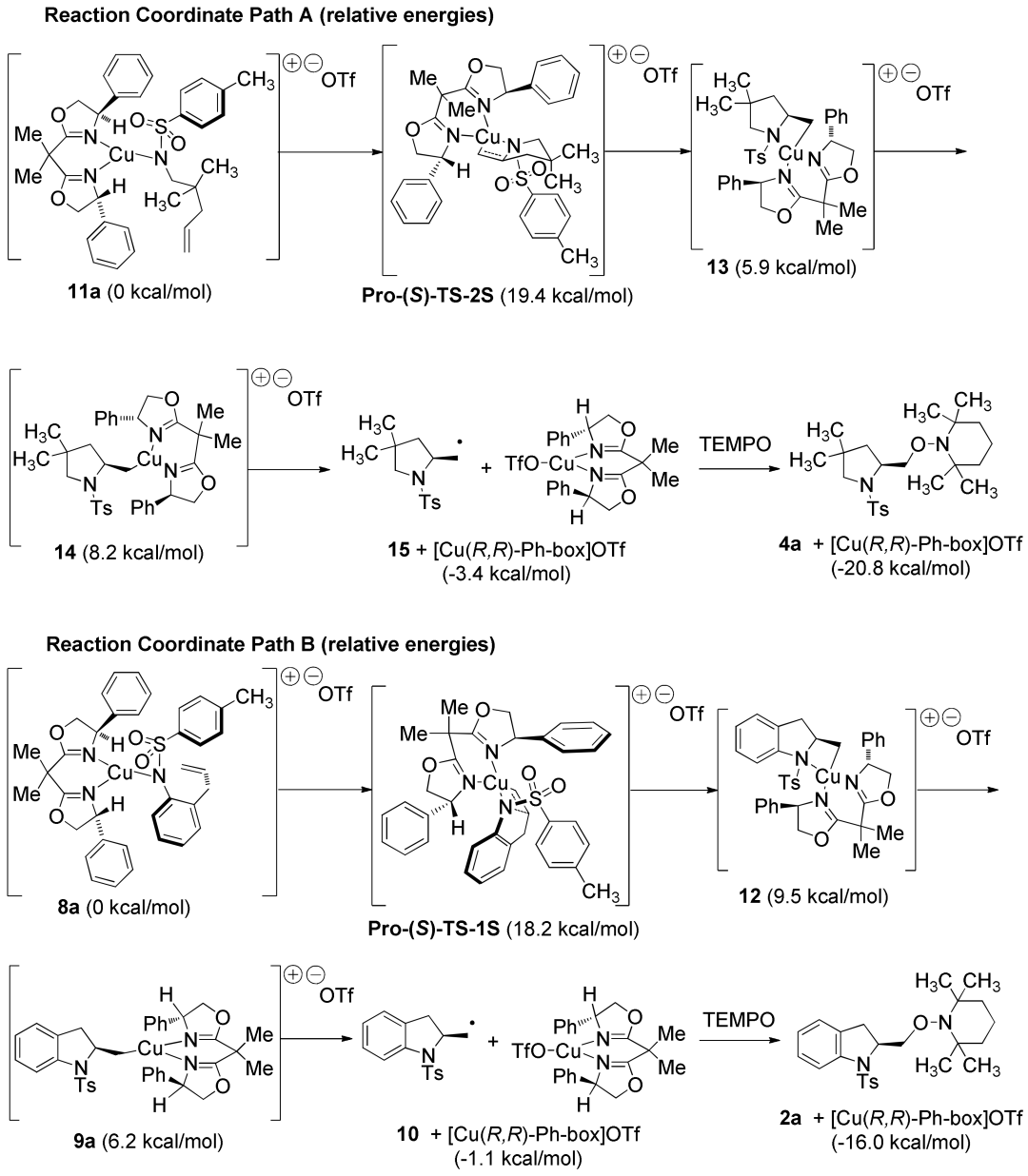

Scheme 2.

Proposed Copper-Catalyzed Aminooxygenation Reaction Coordinates. Pathway A is for the *N*-tosyl-2,2-dimethylpentenamine **3a** and Pathway B is for the *N*-tosyl-*o*-allylaniline **1a**.

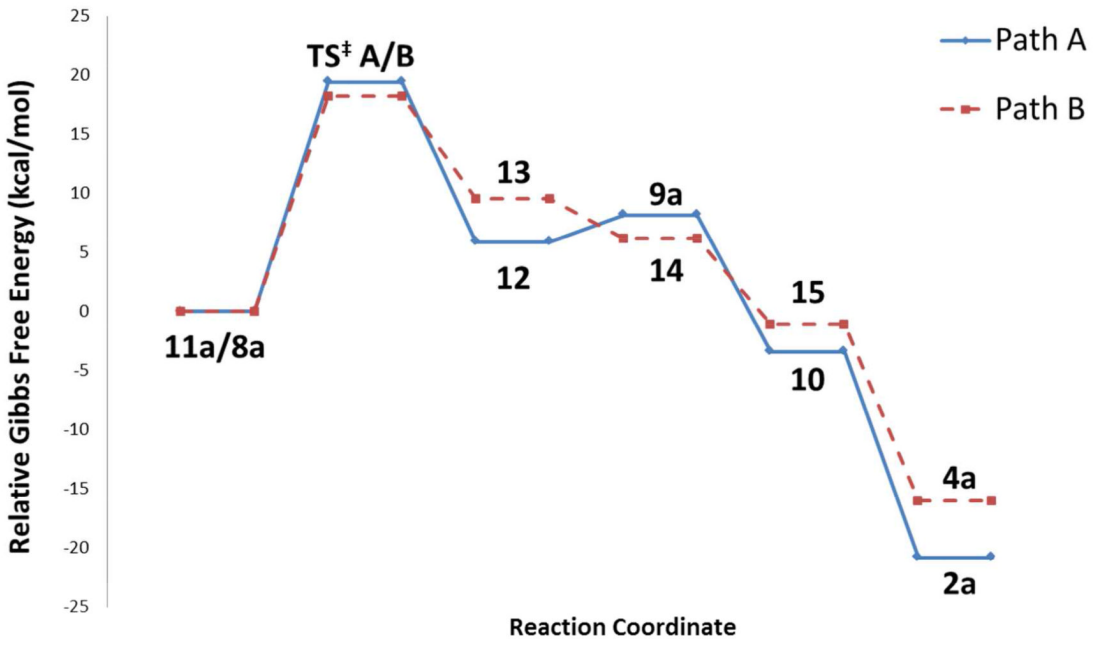

Figure 9.

Calculated free energy profile for the Cu(II) bis(oxazoline)-catalyzed aminooxygenation of *N*-tosyl 2,2 dimethylpentenamine (substrate **3a**, Path A) and *N*-tosyl-*o*-allyl aniline (substrate **1a**, Path B).

Table 1

Tetrahedral twist angles (θ_{TTA}), Selected NBO donor – acceptor stabilization energies, and selected bond distances in **TS-1S**, **TS-1R**, **TS-2S**, and **TS-2R**.

	E_{NBO} (kcal/mol) (corresponding bond distances)			
Transition State	**C_{sub1}–C_{sub2} → Cu**	**N_{sub} → Cu**	**N_{sub} → C_{sub1}–C_{sub2}**	**θ_{TTA}**
TS-1S	12.13 (2.12 Å)	11.28 (2.18 Å)	30.84 (2.05 Å)	26.25 °
TS-1R	9.17 (2.16 Å)	10.07 (2.08 Å)	25.80 (2.08 Å)	50.45 °
TS-2S	10.45 (2.13 Å)	11.15 (2.14 Å)	25.70 (2.09 Å)	13.38 °
TS-2R	8.64 (2.17 Å)	12.64 (2.09 Å)	25.91 (2.10 Å)	44.21 °

Table 2

Tetrahedral twist angles (θ_{TTA}), and selected bond distances in **TS-3S**, **TS-3R**, **TS-4S**, **TS-4R**, **TS-5S**, and **TS-5R**.

Transition State	C_{sub1}-Cu	N_{sub}-Cu	$(C–N)_{sub}$	θ_{TTA}
TS-3S	2.14 Å	2.14 Å	2.08 Å	12.98 °
TS-3R	2.17 Å	2.09 Å	2.10 Å	23.22 °
TS-4S	2.15 Å	2.13 Å	2.07 Å	12.78 °
TS-4R	2.08 Å	2.08 Å	2.08 Å	42.33 °
TS-5S	2.14 Å	2.11 Å	2.08 Å	7.78 °
TS-5R	2.18 Å	2.07 Å	2.10 Å	51.4 °

Table 3

Selected Mulliken Charges in **TS-3S**, **TS-3R**, **TS-4S**, **TS-4R**, **TS-5S**, and **TS-5R**.

Transition State	$N_{lig(1)}$	$N_{lig(2)}$	Cu	N_{sub}	C_{sub2}	C_{sub1}	S
TS-3S	−0.467	−0.474	0.394	−0.671	0.068	−0.483	1.295
TS-3R	−0.463	−0.465	0.353	−0.672	0.048	−0.548	1.288
TS-4S	−0.467	−0.459	0.379	−0.672	0.067	−0.480	1.316
TS-4R	−0.469	−0.464	0.316	−0.669	0.046	−0.449	1.319
TS-5S	−0.463	−0.466	0.417	−0.661	0.069	−0.478	1.303
TS-5R	−0.456	−0.473	0.382	−0.670	0.049	−0.456	1.306